Journal of The Electrochemical Society

The Electrochemical Society
Advancing solid state & electrochemical science & technology

Investigations into the Dynamic Acoustic Response of Lithium-Ion Batteries During Lifetime Testing

To cite this article before publication: Elias Galiounas *et al* 2024 *J. Electrochem. Soc.* in press https://doi.org/10.1149/1945-7111/ad5d21

Investigations into the Dynamic Acoustic Response of Lithium-Ion Batteries During Lifetime Testing

Journal:	*Journal of The Electrochemical Society*
Manuscript ID	JES-112297.R1
Manuscript Type:	Research Paper
Date Submitted by the Author:	15-Jun-2024
Complete List of Authors:	Galiounas, Elias; University College London, Chemical Engineering Iacoviello, Francesco; University College London, Chemical Engineering Mirza, Mateen; University College London, Chemical Engineering Rasha, Lara; University College London, Chemical Engineering Owen, Rhodri; University College London, Chemical Engineering Robinson, James; University College London, Chemical Engineering Jervis, Rhodri; University College London, Chemical Engineering; The Faraday Institution,
Keywords:	Lithium ion batteries, Acoustic testing, Ultrasonic testing, Degradation, Chemomechanics, Acoustic sensitivity analysis

Investigations into the Dynamic Acoustic Response of Lithium-Ion Batteries During Lifetime Testing

Elias Galiounas,[1] Francesco Iacoviello,[1] Mateen Mirza,[1] Lara Rasha,[1,2] Rhodri E. Owen[1,2,3] James B. Robinson[1,2,3] and Rhodri Jervis[1,2,z]

[1]Electrochemical Innovation Lab, Department of Chemical Engineering, University College London, London, WC1E 7JE, United Kingdom
[2]The Faraday Institution, Quad One, Harwell Science and Innovation Campus, Didcot, OX11 0RA, United Kingdom
[3]Advanced Propulsion Lab, Marshgate, University College London, London, E20 2AE, United Kingdom

[z]E-mail: rhodri.jervis@ucl.ac.uk

Abstract

Techniques using acoustic waves to interrogate batteries are increasingly investigated in the literature due to the appeal of three main properties: they are non-destructive, relatively low cost and have acquisition rates enabling operando testing. Popular demonstrations attempt to extract degradation markers from acoustic data, by continuous monitoring, and to attribute them to degradation modes. This is founded on the premise that the speed of sound depends on mechanical properties, such as the density and stiffness. Nevertheless, additional sensitivities of an acoustic time-of-flight analysis are often neglected, leading to incomplete experiments that can overstate the capabilities of the technique. In this work, such sensitivities are quantified and the use of pulse tests instead of CCCV protocols is recommended to elucidate the concurrent dynamic evolution of temperature, voltage and acoustic signals. A degradation experiment is performed, with pulse sequences incorporated in periodic reference performance tests. Dynamic parameters are extracted from each pulse; specifically, the dynamic rise of the time-of-flight (ΔToF_{rise}) and temperature ($\Delta Temp_{rise}$) signals. Their evolution with degradation is traced and a statistical comparison of the main effects is performed. It is concluded that markers of degradation in the dynamic acoustic response are very subtle, masked by the effects of temperature.

1 Introduction

Ultrasonic testing of batteries has attracted increasing attention in the last decade. Early demonstrations can be traced to Sood et al. [1], with the technique becoming cemented with the works of Hsieh et al. [2] and Bhadra et al. [3,4]. The term 'electrochemical-acoustic time-of-flight analysis' was put forward by them. Time-of-flight (ToF) is an elastic phenomenon, characterising the speed of sound in a material, in contrast to acoustic pressure or amplitude which exhibits more complex behaviour. Professional standards [5–7] and textbooks [8] can offer useful insights into acoustic wavefront dynamics, which are often oversimplified in studies performing amplitude- rather than ToF-based analysis. Laminate targets such as batteries give rise to added complexity compared to homogeneous targets, due to the attenuative and reflective nature of their interfaces.

Two research directions that are believed to be promising are the imaging of battery cells using acoustic signals, and the monitoring of formation and degradation markers from acoustic signals—possibly attributing those markers to degradation modes. In spite of much progress that was made in both areas, a more thorough account of the sensitivities that act on the acoustic response is needed in order to assign acoustic features to depth coordinates, or to assert the causality of degradation.

Acoustic imaging can be performed using bespoke setups [9,10], or also with high resolution commercial instruments known as Scanning Acoustic Microscopes (SAM). SAM is an established technique, whereby the surface of a sample is traversed and rasterised images are produced by assigning colour to acoustic characteristics such as the acoustic amplitude at various time gates. Depending on the surface being traversed, images representing cross-sections parallel to the surface, or across the surface, can be produced. These are useful in quality assurance, even though the depth they represent is generally not known with precision. For depth to be computed, the exact geometry and acoustic properties of all layers need to be known, and these have some dependency on the local state-of-charge and health of a battery. A convincing demonstration of SAM applied to batteries is provided by Bauermann et al. [11], where it is also shown that successive layers project information onto one another. Therefore, a matching of acoustic features to depth is challenging.

The isolation of specific interfaces in spite of this projection is actively pursued in the literature, for example by signal transforms [12]. Huang et al. [13] examined how interfacial reflections could constructively interfere forming peaks in the acoustic response. However, assigning every observed peak to a specific interface is likely unrealistic, since the pulsed waveform itself contains multiple cycles and therefore multiple peaks (SI Section 1).

Studies on continuous monitoring of battery cells more commonly employ single-point acoustic monitoring rather than spatial acoustic imaging, possibly due to its simplicity, lower cost and speed advantage. Knehr et al. [14] used continuous monitoring to study cells during their 'break-in' period defined, in this instance, as the first 20 cycles of operation approximately. Significant shifts in the ToF towards higher values were measured during this stage, indicating a change in mechanical properties, or a change in the cell geometry, or both. Battery swelling was observed, and quantification of the degree of swelling was required to deconvolute the two effects. In their work a micrometer was used to measure the thickness of the cell although this risks local compression of its components, potentially offsetting the measurement, especially if gas was present within the microstructure.

Bommier et al. [15] attempted to monitor formation of a solid electrolyte interphase (SEI) in full cells with composite silicon-graphite anodes during long-term cycling. Their observations were two-fold. The ToF shifted upwards with cycling, and the silicon SEI became progressively thicker with cycling as revealed by post-mortem analysis. The ToF shift during the first cycle was attributed to gas formation, but beyond that the continuation of the ToF shift was attributed to a decrease in the cell's effective stiffness associated with continuous thickening of the SEI. However, a progressive expansion of the whole cell would have the same effect on the ToF and in the absence of a thickness measurement it should not have been ruled out. Several degradation mechanisms, other than SEI build-up, can cause cell expansion. For example, continuous gas formation, electrode flaking, particle cracking [16], or delamination. Asserting causality in this case is therefore challenging.

In a similar study on lithium plating [17], the ToF difference between the endpoints of a single full-charge was used as the acoustic metric of interest. This is a relative metric, in contrast to the absolute value of the ToF or signal amplitude. As such, it does not suffer from the long-term accumulation of thickness changes which occur with progressive cycles. In order to promote lithium-plating the authors employ a fixed capacity constant current protocol, although this violates voltage limits. Moving to progressively higher C-rates, a significant acoustic footprint is observed and is attributed to lithium-plating. The authors acknowledge most caveats of their approach, for example the likely acceleration of SEI formation at high voltage, and the dynamic effects of temperature which could have been quantified more rigorously. An aspect not considered is the mechanical effect that high C-rates alone could have, which could potentially cause dynamic stress evolution and acoustic shifts similar to those observed.

In the work presented here the dynamic nature of the acoustic response of batteries is investigated, which exhibits evolution and relaxation characteristics akin to the voltage and temperature. Identification of waveform peaks is employed to reduce the acoustic waveform into features that can be more conveniently visualised against other factors of interest. At first, the sensitivity of the acoustic response to undesirable experimental and methodological factors is demonstrated, as this is incompletely explored in the existing literature. This includes the sensitivity to temperature variation, to the ageing of the acoustic couplant, and to the signal processing technique being employed. The study proceeds to demonstrate the effects of various C-rates on the acoustic response of a pristine cell and shows that they are likely explainable by temperature.

Primarily, this study investigates whether markers of degradation are present in the acoustic response of a full cell during pulse tests. A degradation experiment is performed, with periodic reference performance tests which are acoustically monitored. The progressive degradation of the cell is evidenced by conventional metrics, namely by its capacity fade trajectory and the evolution of electrochemical impedance spectra. Acoustically, although large ToF shifts take place with progressive degradation, as was shown by other authors previously [2,14,18,19], those contain the strong influence of cell-level thickening. This is demonstrated by *in-situ* X-ray computed tomography (CT). Additionally, it is shown that the imperfect control of temperature, which is often inevitable in laboratory testing, can influence the acoustic response significantly and be erroneously interpreted as a permanent mechanical change. To mitigate the influence of cell thickening, and to make temperature effects tractable, the use of pulse tests is recommended and demonstrated. The study reveals that when the effects of cell thickening are minimised, and the effects of temperature are discounted, degradation markers which concern the dynamic behaviour of cells are only weakly present in the acoustic signal.

The data generated in this work is shared [20] open access, as well as the code used in processing, visualisation and animation of the data. This code is in the form of a purpose-built python package titled SonicBatt [21]. The reader is encouraged to follow the instructions in the SonicBatt repository to reproduce the main plots of this study.

2 Experimental methods

2.1 Cell chemistry, cycling and temperature control

Commercial cells with a nominal capacity of 210 mAh and $LiCoO_2$/Gr chemistry (Model 651628, AA Portable Power) were used. A complete specification sheet is provided in the Supplementary Information (SI). The same cell was used in several other acoustic studies [17–19,22–24], and its detailed chemical composition can be found in two of them [19,23]. Cycling was performed with a computer-controlled potentiostat (1010E, Gamry instruments, US). The surface temperature was monitored with an N-type thermocouple, attached to the surface of cells using polyamide adhesive tape, and using a TC-08 thermocouple interface (Pico Technology, UK). The ambient temperature was controlled, except in X-ray experiments, by placing cells inside one of two temperature chambers. Specifically, an Espec SU-242 environmental chamber was used for the sensitivity experiments of Section 3, and a Maccor MTC-020 chamber was used for the degradation experiment of Section 4. The temperature setpoint was set to 25 °C for all experiments except for the variable temperature study of Section 3.2. All cycling was performed between the manufacturer's stated voltage limits of 2.75 and 4.2 V. Prior to recording any of the presented data, cells underwent a small number of slow cycles (2-5 cycles at a rate of C/20 or C/5) to ensure electrode rewetting and complete formation.

2.2 Electrochemical Impedance Spectroscopy (EIS)

Potentiostatic EIS experiments were performed over the frequency range of 100 kHz to 10 mHz measuring 15 points per decade using a 10 mV RMS perturbation.

2.3 Acoustic testing

Acoustic data was acquired using an Olympus 650 ultrasonic flaw detector and a single 6 mm diameter, 5 MHz transducer operating in pulse-echo mode (M110-RM, Evident Scientific). The transducer was secured by a 200 g weight. Acoustic experiments on any one cell were always conducted to completion without moving the transducer. This includes the long-term degradation experiments that will be discussed. The pulsing settings used are stated in Table 1 — these settings are specific to the Olympus flaw detector. A small amount of silicon-dioxide-based couplant (couplant H-2, Evident Scientific) was applied between the transducer and the cell. The pulsing frequency during battery experiments was set to a value different from the transducer's centre frequency, i.e., 2.25 MHz instead of 5 MHz. This is generally not advised; however, consistent waveforms can be produced regardless and a comparison can be made using SI Figure 2 and SI Figure 3.

Table 1: Ultrasonic flaw detector settings

Energy	300 V
Gain	51 dB
Range	10 µs
Filter	0.5–4 MHz
Pulse frequency	2.25 MHz

To investigate the shape of the pulsed waveforms, and the effects of various bandpass filters, a 100 mm thick block of aluminium was used to record waveforms in pulse-echo mode. The use of a thick target allowed the clear separation of the first 'back wall echo' from subsequent echoes, and the waveform corresponding to a single acoustic pulse was windowed. The experimental setup and waveform recordings are shown in SI Section 1, also demonstrating the effect of the chosen bandpass filter of 0.5–4 MHz.

A typical waveform obtained from a battery scan, in the form of an amplitude versus time scan (A-scan), is shown in Figure 1. The time-increment resolution is 2.5 nanoseconds, i.e., the sampling rate when recording a single waveform is 400 mega samples per second (MS s^{-1}). Amplitude is measured in arbitrary units and can attain integer values between 0 and 511. The maximum acquisition rate for complete waveforms was approximately 1 waveform per second. This rate was varied during experiments to ensure that the size of the acquired dataset was manageable while still using the fastest rate during dynamic events. The ToF (horizontal) positions of the 9 peaks shown in Figure 1 were identified, for all signals. Other peaks could not be identified robustly at all cycling conditions because their prominence was not always adequate. For the peak identification to be done robustly, it was necessary to first perform a smoothing operation involving multiple passes of a moving average kernel over each signal. The smoothing was then discarded, retaining the identified peak ToFs and the respective amplitudes on the original signal. Smoothing parameters themselves can influence the position of the identified peaks, as described in SI Figure 4 and SI Figure 5. It is henceforth assumed that by using consistent smoothing parameters, throughout this work, any distortion effects are also consistent. The amplitude of successive peaks follows a decaying pattern due to signal attenuation, with the exception of the final peak which is widely accepted to originate at the posterior side of the cell. The large mismatch in the acoustic impedance across that interface is believed to produce a more pronounced peak, as seen. This peak is often termed the 'back-wall echo'.

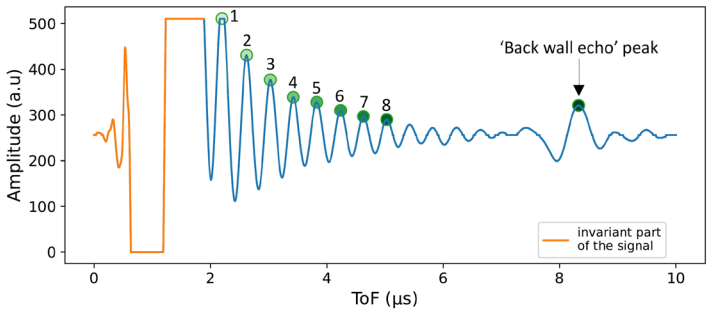

Figure 1: Example acoustic signal recorded from a battery scan, with 9 identified peaks. The 'back wall echo' peak is primarily used in subsequent analysis. The first 8 peaks are used solely in the variable temperature study, where they are also designated by their shaded green colours. Only 8 of these 'early peaks' are studied because subsequent peaks (except the 'back wall echo') could not be identified robustly at all states-of-charge.

The ToF of this final, back-wall echo, peak is the primary acoustic feature used in this study. Reducing the entire acoustic waveform into this feature aids visualisation and is a useful simplification when studying acoustic shifts. Figure 2 demonstrates a typical dynamic test conducted in this work, in the form of a constant current pulse preceded and followed by rest at open circuit. The ToF shown is that of the 'back wall echo' peak. The ToF is seen to evolve dynamically similar to the voltage and to the temperature. Figure 2 defines terminology that will be used extensively in the sections that follow. Particularly important are the rise levels of the ToF (ΔToF_{rise}) and temperature ($\Delta Temp_{rise}$), the open circuit voltage (OCV) before the pulse and the average temperature measured over 5 minutes before the pulse (T_0). ToF and voltage retain a permanent shift at the end of the relaxation period due to the arrival at a new state-of-charge (SoC). All pulses discussed in this work deplete 10.5 mAh at constant current, regardless of the C-rate. This amounts to 5 % of 210 mAh - the specification capacity of a pristine cell. Each pulse was preceded by 5 minutes of rest, and was followed by approximately 75 minutes of rest. An animation showing how the acoustic signal evolves during an example sequence of pulses can be found in the SI.

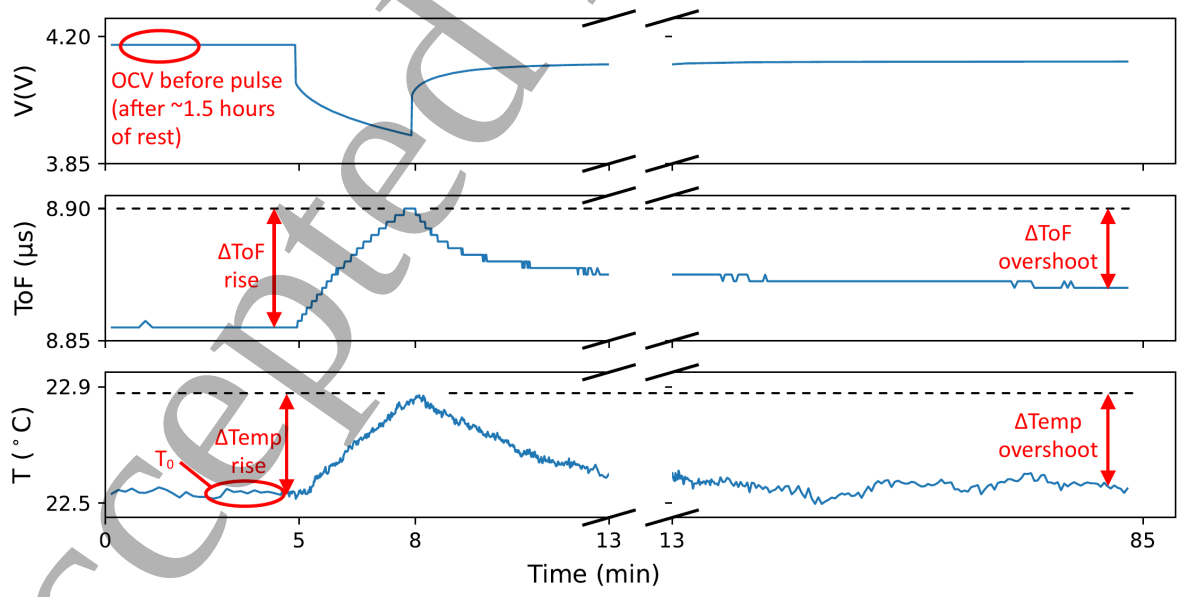

Figure 2: Example of pulse-relaxation event with monitored voltage, acoustic and temperature signals. The acoustic signal is specifically the ToF of the 'back wall echo' peak. Designations show signal features used in subsequent analysis.

2.4 X-ray Computed Tomography

A Nikon XT H 225 X-ray tomography scanner (Nikon Metrology, Tring, UK) was used to obtain tomograms from the middle region of the cell. The settings stated in Table 2 were used to acquire the tomograms. The duration of a single scan was approximately 15 minutes. A complete experiment involved a total of 22 scans, starting with a fully charged cell, and depleting its charge incrementally. Charge was removed in increments of 10.5 mAh (5 % of 210 mAh), at a rate of 0.5 C. After 20 such discharges, a final discharge at 0.2 C was performed until the lower voltage cutoff was reached. The intent of the final discharge was to approach the bottom-of-charge more closely by causing a lower overvoltage thanks to the lower C-rate. Each discharge was followed by at least 1.5 h of rest at open circuit conditions. Sometimes the rest was overnight, as a complete experiment lasted approximately 3 days with pauses during night time.

To allow the cell to be discharged without disturbing its position, a slip-ring assembly was used (Figure 3a). The cell was placed inside a 3D printed holder and was secured with a small piece of foam. The foam exerted minor pressure on the cell, but the influence of this light compression on the cell's ability to expand and contract is believed to be minimal. The distance between the cell and the X-ray source was adjusted so that the pixel size was approximately 6.85 µm. This pixel size was later scaled, during post-processing, according to calibration scans that were performed on a 2 mm calibration steel rod. The above procedure was performed, in its entirety, twice. Initially on a pristine cell, and later on the same cell after degradation cycling. By post-processing the tomograms, the relationship between SoC and thickness was quantified for the cell in its pristine and aged conditions.

Table 2: X-ray CT settings

Beam Energy	225 kV
Current	61 µA
Exposure time	267 ms
Projections	3185

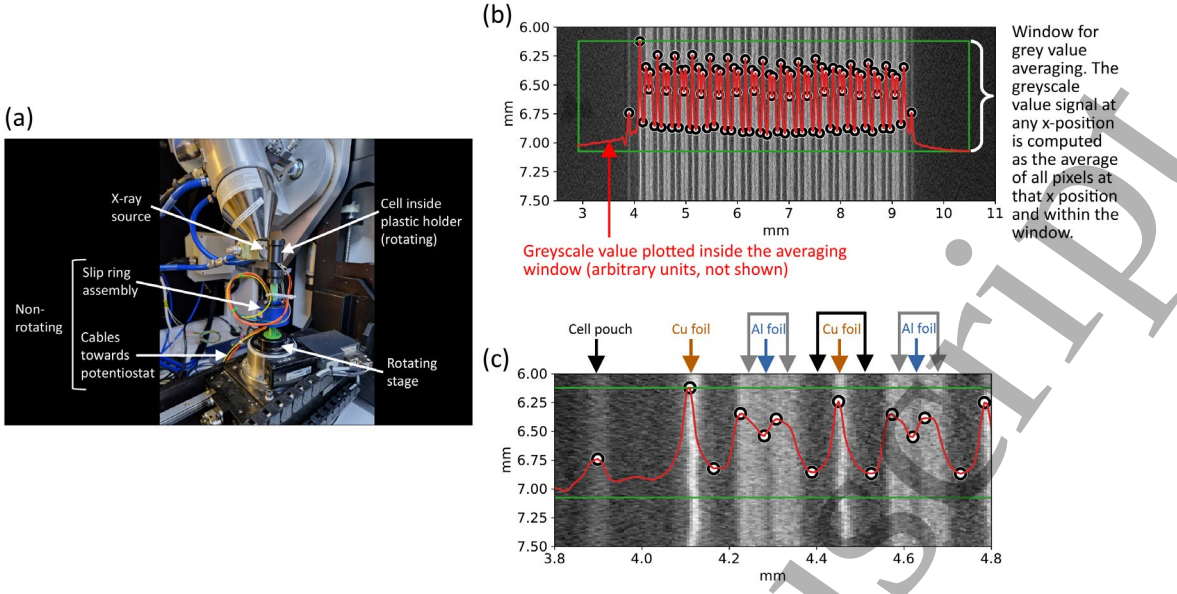

Figure 3: In-situ X-ray computed tomography. (a) Experimental setup. (b) Cell cross section, showing the full cell thickness and an example signal of the greyscale value with identified peaks. The height of the green window shows the amount of material over which the greyscale value was averaged. (c) Close-up of the tomogram and material designations.

The tomograms were processed in Fiji ImageJ by isolating a region from the middle of the cell as shown in SI Figure 6. A brightness adjustment was initially performed, followed by the acquisition of greyscale values along multiple paths spanning the cell thickness. To produce uncertainty bounds concerning the influence of cell alignment on the thickness measurements, the following process was followed. Images were first rotated so that the cell layers were close to vertical. A one degree rotation was then applied, both in the clockwise and anticlockwise directions, producing two image variants that were slightly tilted on each side of the vertical plane. On each of the two rotated images, greyscale values were measured along three paths (SI Figure 7), i.e. at each SoC a total of 6 greyscale signals were processed.

To improve the smoothness of the greyscale signal, the greyscale value was averaged over a windowed region of rectangular shape. This is believed to be more robust than the alternative of obtaining greyscale values along a line. An example of a greyscale signal, acquired as described above, is shown in Figure 3b-c together with the identified signal peaks. Peaks were particularly pronounced at the copper current collectors, which appear bright in the scans, and at the pouch material present at the front and back. The locations of the first and last peaks, which correspond to the cell pouch, together with the calibrated pixel size, were used to measure the cell thickness at various states-of-charge. This attempt to quantify thickness changes using tomography differs from the work of Chang et al. [19] who used radiography. Animations of the sequence of tomograms, for the pristine and aged conditions, are provided in the SI.

3 Sensitivities

3.1 Sensitivity to couplant ageing

The study of cell degradation requires long-duration experiments. It is therefore essential to investigate whether the passage of time alone affects the acoustic signal. This could be the case if the acoustic couplant changes in its consistency. Trial tests using a glycol-based couplant (Couplant D12, Evident Scientific) inside a temperature chamber at 25 °C resulted in a complete loss of signal after 2-3 days due to the couplant drying out under convection. This study uses a silicon-dioxide-based

couplant, which is recommended for high-temperature use. To investigate its stability, one cell was monitored acoustically for 24 days at open-circuit conditions and with the temperature controlled at 25 °C. The stability of the voltage and temperature can be visualised in SI Figure 9. The amplitude and ToF changes for the identified peaks can be seen in SI Figure 10. The peak characteristics change primarily during the first 2 days and then largely stabilise. The maximum percentage change in ToF was 0.6 %, while the maximum percentage change in the amplitude was an order of magnitude greater. Considering the percentage change, instead of the absolute change, of these quantities allows a comparison between them to be made. This provides further justification to favour ToF over amplitude as the monitoring feature, in addition to the ToF being more comprehensible due to its elastic origins. In absolute rather than percentage terms, the maximum change in the ToF of any peak was 0.025 µs compared to the respective value on Day 1. This value is approximately the same for all peaks, which is logical because changes to the acoustic couplant affect the signal only before and after it has travelled through the cell.

3.2 Sensitivity to temperature

A different cell, with a voltage of ca. 4.1 V, was subjected to a controlled temperature variation while its open-circuit potential and acoustic behaviour were monitored as dependent variables. Temperature was varied in the range of ca. 11.5 to 31.5 °C, in increments of approximately 2.5 °C as shown in Figure 4. Changes to the temperature setpoint were applied gradually as linear ramps, taking 1 hour to reach the new setpoint. At each setpoint the temperature was held constant for 3 hours. The colourmaps of SI Figure 11 demonstrate the respective acoustic changes.

The amplitude and ToF of the identified peaks are plotted in Figure 5 against the temperature. The absolute and percentage changes relative to the minimum temperature are also shown. The amplitude of Peak 1 was saturated for part of the temperature range, having attained the maximum value that the equipment can record. Amplitude and temperature appear to be inversely related, for all peaks. The slope differs for each peak, and there is no relationship between the slope and the peak rank (first peak, second etc). This contrasts with the ToF, which increases universally with temperature and later peaks are affected more than earlier peaks (Figure 5d). The ToF dependence on the temperature can be justified in two ways. The cell thermally expands; or the speed of sound changes as a function of temperature; or both. Additionally, the higher sensitivity of the later peaks to temperature can be explained by assuming that later peaks represent positions deeper within the cell. Under these assumptions, and if cell expansion was uniform, the percentage change in ToF should be identical for all peaks as the calculation of the percentage change normalises the ToF of each peak by its value at the minimum temperature. This is equivalent to normalising by the depth coordinate of each peak at the minimum temperature, and therefore overlapping lines should be expected in Figure 5f. Instead, divergence is observed for the different peaks. This divergence likely suggests that geometric changes due to thermal expansion are not uniform. It is possible that the cell bulges as it expands, resulting in a movement of cell layers which differs depending on their depth.

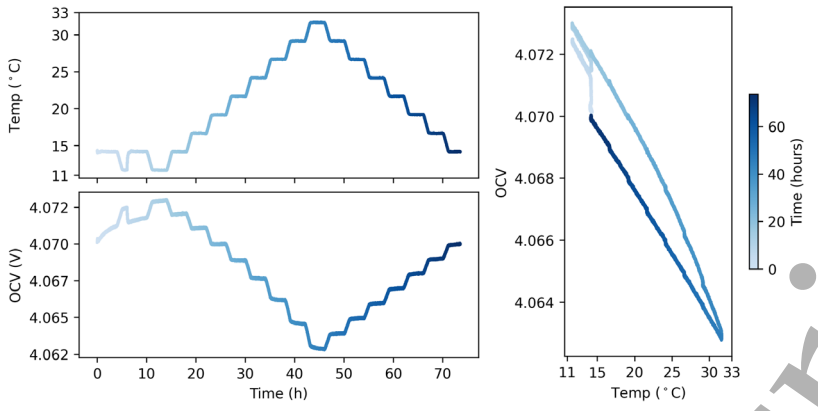

Figure 4: Temperature variation experiment. Temperature is controlled. OCV is monitored. The acoustic response is also monitored and shown in Figure 5.

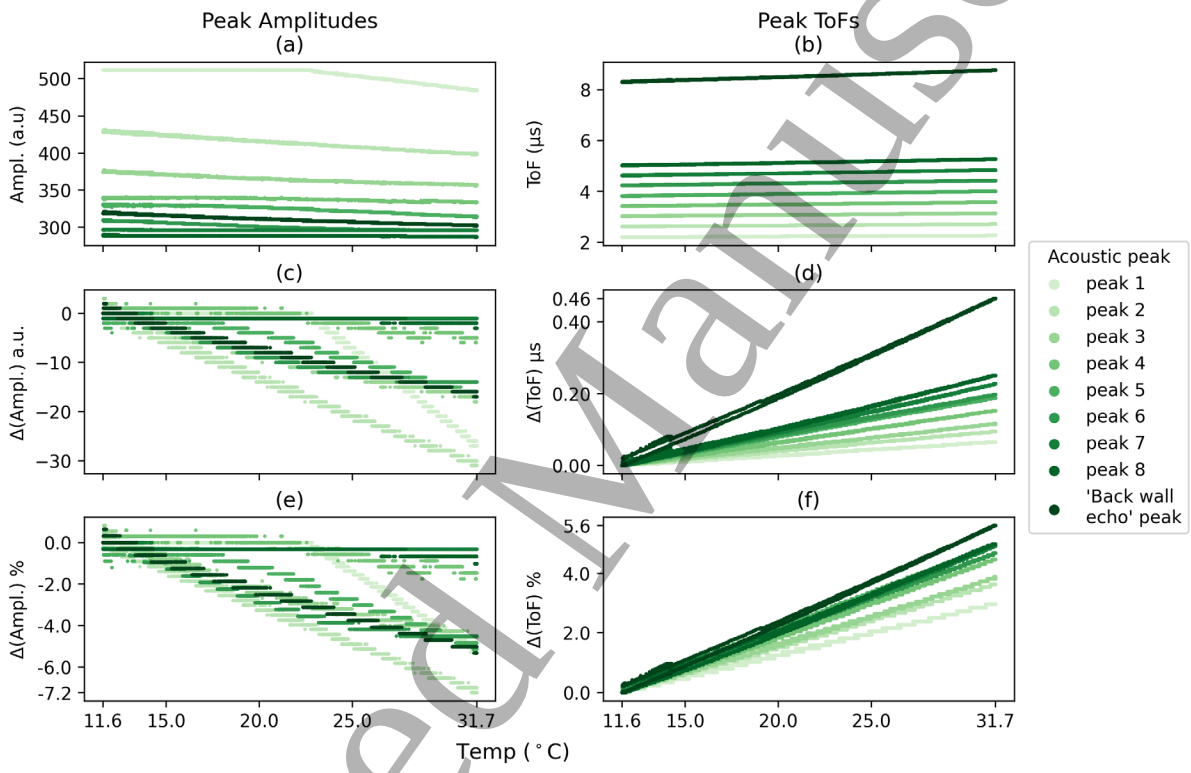

Figure 5: Temperature variation experiment. Sensitivity of peak amplitude and peak ToF to temperature.

To demonstrate how homogeneous thermal expansion would result in overlapping lines in Figure 5f, a one-dimensional model of an idealised cell was created. The model applies a simple discretisation scheme through-the-thickness (SI Figure 12), allowing through-thickness variation of temperature and consequently of strain and speed of sound. The model assumes that the battery is made of a single homogeneous material, and allows the coefficients controlling thermal expansion and speed of sound, to be perturbed. The model is provided with the SonicBatt repository [21] as an interactive tool, and illustrative plots are shown in SI Figure 13 and SI Figure 14.

Beyond the temperature sensitivities discussed, it can be logically argued that the acoustic transducer itself may be sensitive to the temperature — not only the test sample. This possibility was not investigated; nevertheless, we consider the inferences made to be appropriate given the available

evidence. A linear relationship between the 'back wall echo' ToF and the temperature was also observed by Owen et al. [24], for a temperature range of 70 °C (-10 to 60 °C), using the same acoustic equipment and cell. Using in-house acoustic equipment, Popp et al. [25] reported a non-linear dependence between a ToF feature and the temperature; however, the feature concerned was not a waveform peak.

It is noted from Figure 5f that the percentage change in ToF caused by a unit change in temperature is in the range 0.13-0.28 % $°C^{-1}$. Specifying this rate as a percentage should be more universal rather than an absolute value, and applicable to other cells of this chemistry and type.

3.3 Sensitivity to the c-rate

The kinematic expression for the ToF is:

$$ToF = \frac{2h}{c} \quad (1)$$

where h is the target thickness and c is the speed of sound through it. The length of travel comprises twice the thickness because of operating in pulse-echo mode. The speed of sound is broadly linked to the material properties by the following statement:

$$c \propto \frac{\text{elastic property}}{\text{inertial property}} \quad (2)$$

and the exact formulation depends on how the material is interpreted. In isotropic solids the expression $c = \sqrt{E/\rho}$ is often used (E = Young's modulus, ρ = density), although it may be more appropriate to use a combination of the bulk and shear moduli as the elastic term, depending on the acoustic wavelength and target dimensions [26]. In liquids only the bulk modulus is defined. Battery electrodes and separators have often been modelled simplistically as solids, or as fluid saturated porous media using Biot theory [13,27], or electrodes specifically as slurries [13]. It is reasonable to postulate that the evolution of mechanical stress in a battery could influence the elastic term, contributing a transient stiffness component to the 'effective stiffness' of the material. The following formulation expresses this.

$$c = \sqrt{E_{eff}/\rho} \quad (3)$$

Robinson et al. [28] used the term 'electrochemical stiffness' for the rate-dependent stiffness, influenced by Tavassol et al. [29], and argued that it is detectable acoustically. However, they dismissed thermal effects. Chang et al. [19] attempted to quantify the evolution of the effective stiffness at different C-rates (1C, 2C and 3C) by performing concurrent acoustic and thickness measurements. A C-rate dependence was observed, however, thermal effects due to Ohmic heating were disregarded, even though Ohmic heating is known to be C-rate dependent itself [30]. Experiments on the same cell by Owen et al. [24] attempted to differentiate thermal from C-rate effects during Constant Current –

Constant Voltage (CCCV) operation. They concluded that no clear C-rate effects were observable in the acoustic response between 0.2 C, 0.5 C and 1 C.

The interplay between C-rate, temperature and acoustic response can be better elucidated using current pulses at multiple C-rates as shown in Figure 6a. All pulses deplete the same amount of charge — 10.5 mAh. Pulses 1–5 are in the discharge direction and Pulse 6 is in the charging direction. It is worth noting that in the charging direction the ToF shifts downwards, opposite to what happens in the discharge direction, nevertheless it experiences an upwards transient. This transient, designated by an asterisk, could be due to the influence of temperature and will be revisited in Section 4.5.

In Figure 6b the relationship between the ΔToF_{rise} and $\Delta Temp_{rise}$ is shown for the discharge pulses. An approximately linear correlation is observed, similar to the linear dependence between ToF and temperature revealed earlier in Section 3.2. If a significant transient stress evolution had taken place, which was different for high vs low C-rates, it would have caused the ToF to deviate from its linear relationship with the temperature. A similar argument can be made when considering the cell thickness, as the linear relationship between temperature and the ToF from Section 3.2 implicitly contains the effects of thermal expansion. If a C-rate dependent cell stiffening had taken place, the respective strain evolution would have also caused a distortion of the relationship between temperature and thickness, therefore also disturbing the linear relationship between temperature and the ToF. This hypothesis could better be investigated if thickness measurements were also obtained dynamically. Dynamic measurements will be the subject of future work, although our study considers thickness measurements at equilibrium in Section 4.3. It is concluded that any transient stress evolution, or in other words any C-rate-dependent stiffening or softening, is either identical for the C-rates tested (0.2 C to 1 C), or it is not present, or it is relatively weak.

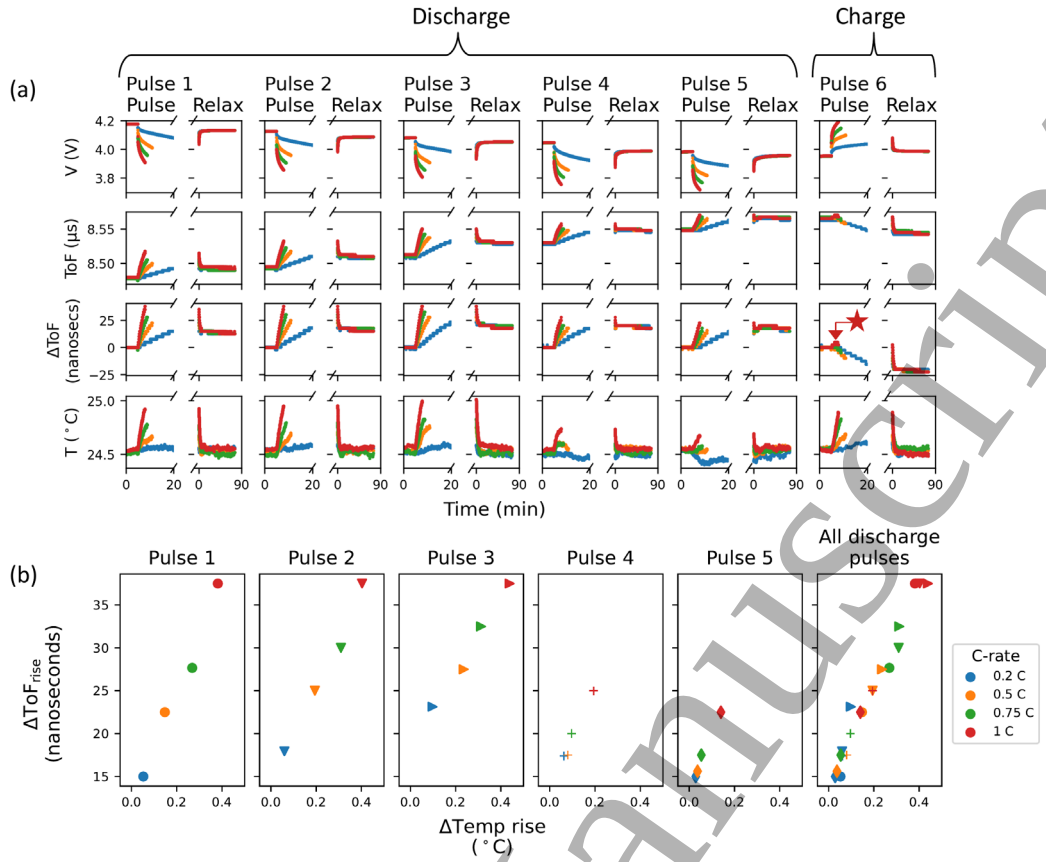

Figure 6: Pulse tests using multiple C-rates. All tests conducted on the same cell. Pulses 1–5 are in the discharge direction. Pulse 6 is a charging pulse. (a) Sensed signals plotted vs time. The asterisk placed on ΔToF of the charging pulse notes an upwards transient shift that takes place before the ToF shifts downwards. (b) ΔToF_{rise} plotted against $\Delta Temp_{rise}$.

4 Degradation Experiment

4.1 Cycling and reference performance tests (RPTs)

The degradation protocol involved cycling at 1C CCCV, with a constant voltage (CV) hold at 4.2V which was terminated once the current decayed to C/20 or after 1.5 hours. A total of 300 cycles were performed and cycling was interrupted every 50 cycles to run a reference performance test (RPT). Five consecutive RPTs were additionally performed after Cycle 300, thus plots concerning the RPTs show data for up to Cycle 305. RPTs included a series of EIS tests and a series of acoustically-monitored pulse tests, all performed at certain OCVs. For these OCVs to be reached with consistency, a long CV hold was used as discussed next. This ensured that the SoC was highly consistent between successive RPTs.

For EIS, the OCVs were 4.2, 4.0 and 3.8 V. For pulse tests, four pulses were performed in the discharge direction, starting at 4.2, 4.0, 3.8 and 3.6 V, and a single pulse in the charging direction starting at 3.6 V. All OCVs were approached with a CCCV protocol, where the constant current was equivalent to C/5 and the CV hold persisted until the current decayed to C/100 or after 3 hours. Upon termination of the CV hold, a 1.5 h rest period followed in all cases. As the cell progressively degraded, the targeted OCVs became more difficult to approach due to a rise in the impedance. This was mitigated by adjusting the voltage values prescribed to the potentiostat for the CV hold in the last half of the experiment. For example, instead of aiming directly for the target OCV of 4.0 V, the value of 3.999 V was used in later RPTs, as this resulted in the voltage arriving at a value closer to the target OCV after

rest. The importance of voltage consistency will be revisited in Section 4.6. Pulse recordings involved 5 mins of rest before pulse initiation, followed by a 3 min pulse at 1C, followed by approximately 75 mins of rest.

4.2 Conventional evidence of degradation

The capacity fade over 300 cycles was ca. 15 %, as shown in Figure 7a. Nyquist plots from the EIS tests reveal an overall increase of the Ohmic resistance of the cell with progressive cycling, as shown in the insets of Figure 7b and in SI Figure 15, with exceptions which can be attributed to coincidentally high temperatures due to the imperfect control of the chamber. It is worth noting that while the Ohmic resistance is seen to increase with degradation, other constituents of the impedance are not. For example, the span of the supressed semicircles along the real axis, which is often associated with the charge transfer resistance [31,32], remained relatively stable after the first RPT. The mechanisms responsible for such changes to the impedimetric profile are also temperature-dependent and generally more difficult to elucidate. Nevertheless, the overall rise in the Ohmic resistance is a clear indicator of a decrease in conductivity which is a degradation marker. Studies suggest this to be primarily caused by electrolyte decomposition, or by the formation of passivation layers on the anode and cathode, or by corrosion of the current collectors [33,34].

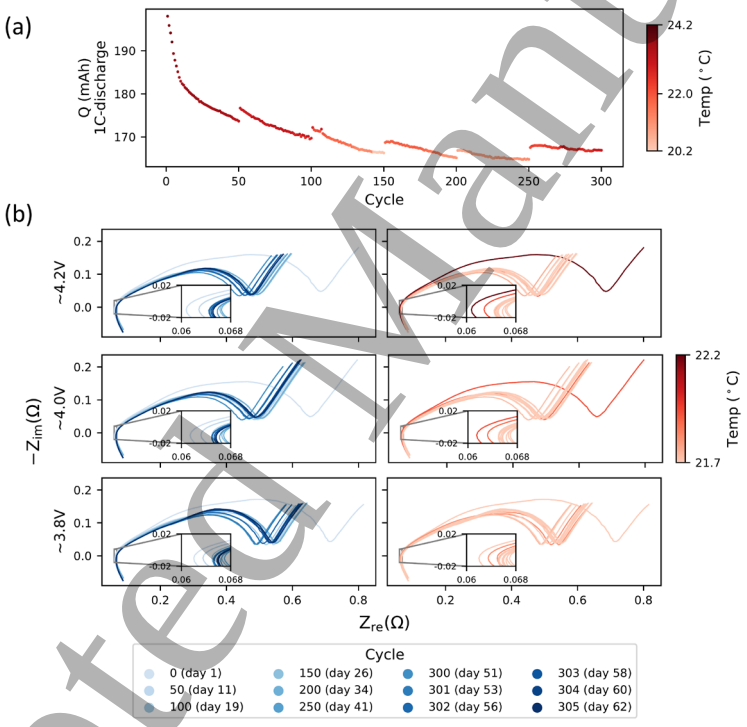

Figure 7: Conventional evidence of degradation. (a) Capacity fade plot at 1C discharge. (b) EIS Nyquist plots obtained at 3 different voltages. Coloured by: cycle number — left column; temperature — right column. The temperatures shown represent the average temperature recorded in the duration of a single EIS test — i.e. each Nyquist curve contains a single colour.

4.3 Thickness variation

Thickness measurements obtained using X-ray CT, before and after degradation cycling and at various states-of-charge, are shown in Figure 8. It is reiterated that these measurements were taken from the same cell. A thickness increase of 3.8 ± 0.5 % was caused by degradation processes (Table 3), measured between the front and back pouch material. The variation of thickness with SoC was also found to be

different between the pristine and aged cases. In the pristine cell, the fully charged state was ca. 3 % thicker than the fully discharged state. The equivalent for the aged cell was ca. 1.5 %. In particular, the sudden thickness increase near the top-of-charge was absent in the aged cell. Given that this was a single- or two-point measurement, and that some measurement noise is observed, it is possibly a measurement flaw. Alternatively, it may indicate that full lithiation of the anode and formation of the LiC_6 intercalation compound is inhibited in the aged cell. The net thickness difference of the aged compared to the pristine condition, of ca. 3.8 %, is more significant than noise and is considered to be a real effect. It is reiterated that the pixel size was calibrated for both the pristine and aged cell scans, using reference scans of a calibration rod. The expansion of pouch cells as they degrade is a known phenomenon and is attributed to a range of factors, including gas evolution, formation of passivation layers, twisting and deformation of cell layers, and swelling due to electrolyte permeation of the binder and separators [35–37].

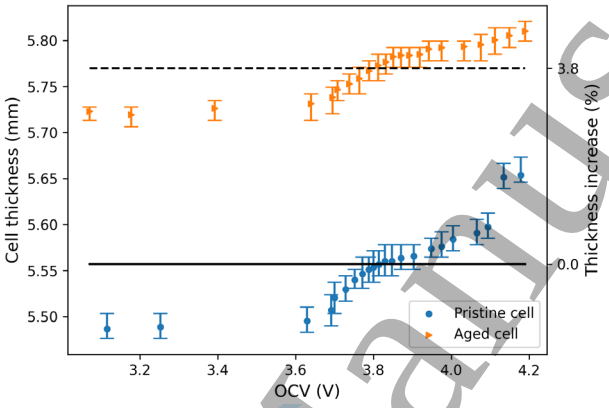

Figure 8: Thickness variation with OCV for the cell in its pristine and aged conditions. Thickness measurements correspond to the distance between the front and back pouch material, obtained by processing of X-ray CT tomograms. Uncertainty bounds originate from measuring greyscale values along 6 paths crossing the cell, and from applying small rotations to the tomograms as discussed in Section 2.4. Markers are placed at the average of these measurements.

Table 3: Change in thicknesses (h) between pristine and aged conditions

	Pristine	Aged	$\frac{h_{pristine}}{h_{aged}}$	$\frac{h_{aged} - h_{pristine}}{h_{pristine}}$
Max h	5.653	5.810	0.973	2.8 %
Min h	5.486	5.723	0.959	4.3 %
Mean h	5.557	5.770	0.963	3.8 %

4.4 Acoustic response

The acoustic response during the RPTs, and the associated voltage signals, are shown in Figure 9. Shades of the blue indicate the number of degradation cycles accumulated up to that point. A net increase in the ToF is observed over progressive cycles, as expected from the discussed literature. This increase occurs for all 5 pulses in a RPT, and it is significantly more sudden in the early stages of the experiment (between cycles 0 and 50), possibly due to an associated expansion of the cell caused by the completion of cell formation which creates SEI and releases gas. This hypothesis is also supported by the pronounced drop in capacity in the first 50 cycles (Figure 7a), where SEI likely forms consuming lithium. Comparing cycle 0 to cycle 305, the ToF increase, averaged over the 5 pulses, is ca. 5.1 % (Table 4). This level of ToF shift is substantially but not entirely explainable by the respective thickness

change according to the framework of Eqns 1–3, and suggests an additional change in the cell's mechanical properties.

By assuming one-dimensional cell expansion, the change in density can be inversely related to the change in thickness and Eqn. 4 can be used to obtain the change in the effective stiffness (derivation in SI Section 7.2). Using maximum and minimum values for $h_{pristine}/h_{aged}$ and $ToF_{aged}/ToF_{pristine}$ from Table 3 and Table 4, the effective stiffness of the aged cell (Cycle 305) can be calculated to be lower than that of the pristine cell (Cycle 0), with the difference being between 7.5 % and 4.9 %. A similar analysis was performed by Chang et al. [19] for the same cell, although the way density was treated is not specified in their study. They observe a 'softening' of the cell by ca. 10.5 % after 15 cycles of operation at 1 C CCCV. This is larger than our calculations; however, their cycling protocol overcharged the cell to accelerate degradation so a strict comparison is not possible.

It should be noted that the accuracy of the thickness measurement, and the assumptions concerning the change in density can significantly influence the computation of stiffness changes. For example, if thickness measurements were -0.22mm and +0.22mm for the pristine and aged conditions respectively, the ToF shift would be entirely explainable by the change in thickness and the associated change in density. Furthermore, there is evidence that temperature also had an effect in our experiment. The effect of temperature can be seen qualitatively by considering Figure 9 (b) and (c) together. In Figure 9b, Cycle 305, which is the final cycle, does not have the highest ToF. From Figure 9c it can be seen that the temperature of some preceding cycles was higher, explaining why their ToF was also higher. Additionally it must be clarified that the term 'stiffness' in the context of acoustic testing represents a bulk property of the cell, and its link to the mechanical stiffness, which is associated with the structural rigidity of a material, is yet to be explored.

The correlation between acoustic features and the state-of-health (SoH) has been attempted in the literature, although not exhaustively. Hsieh et al. [2] showed a qualitative correlation in the cycling behaviour of a cylindrical 18650 cell over 75 cycles, and Davies et al. [18] attempted to quantitatively link the acoustic response to the capacity fade of three pouch cells over 300 cycles. In Davies et al. the cells used are identical to ours, and the clearest trend observed is that the ToF shifts towards greater values with progressive cycling. The authors computed ToF relative to a reference signal using a convolution operation instead of monitoring a signal peak. The two methods seem largely interchangeable. Given our comments on the influence of cell thickening and temperature, we are motivated to attempt a deconvolution of the thickness and temperature effects from any residual acoustic signs of degradation during pulse tests. If such acoustic signs of degradation are present, they will suggest a change in the mechanical dynamics of a degrading cell which is detectable by acoustic testing.

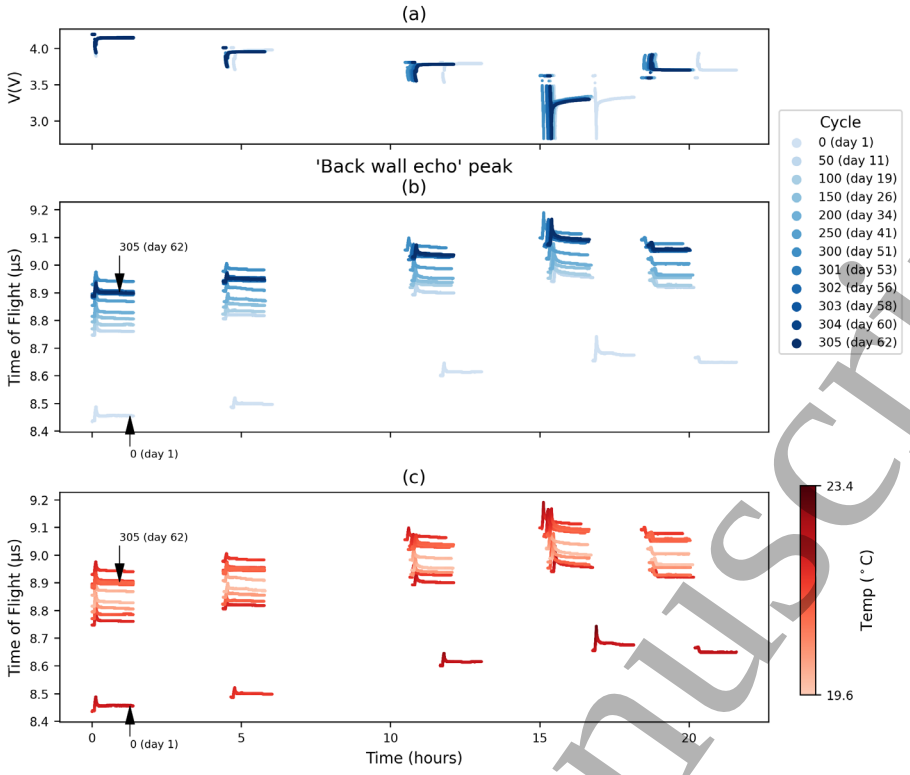

Figure 9: Pulse-relaxation data obtained during reference performance tests. (a) Voltage data coloured by the cycle number. (b–c) Acoustic ToF of the 'back wall echo' peak, coloured by the cycle number in (b) and temperature in (c).

Table 4: Change in ToF between pristine and aged conditions. Cycles 0 and 305 are treated as the pristine and aged conditions respectively. ToF values are reported as the average of the 5-minute rest period before each pulse.

	$ToF_{pristine}$	ToF_{aged}	$\frac{ToF_{aged}}{ToF_{pristine}}$	$\frac{ToF_{aged} - ToF_{pristine}}{ToF_{pristine}}$
Pulse 1	8437.287	8887.609	1.054	5.34 %
Pulse 2	8485.729	8940	1.054	5.35 %
Pulse 3	8600.111	9030	1.050	5.00 %
Pulse 4	8655.056	9076.667	1.049	4.87 %
Pule 5	8665.000	9072.500	1.047	4.70 %

$$\frac{E_{pristine}}{E_{aged}} = \left(\frac{ToF_{aged}}{ToF_{pristine}}\right)^2 \frac{h_{pristine}}{h_{aged}} \in [1.051, 1.081\,] \quad (4)$$

$$\Rightarrow \frac{E_{aged} - E_{pristine}}{E_{pristine}} \in [-7.5\,\%, -4.9\,\%\,]$$

4.5 Search for degradation features in the dynamic acoustic response

Rebaselining the ToF and temperature before each pulse to zero, Figure 10 shows the dynamic rise and relaxation characteristics over progressive cycles, i.e. as the cell degrades. To set the zero baselines, the 5-minute rest preceding each pulse was used to compute the average ToF and temperature, and shift the pulse data accordingly. The recordings of the acoustic signal overlaid in this way show only subtle changes with degradation. Temperature measurements were more noisy than

acoustic measurements, and fluctuated over time due to the imperfect control of the environmental chamber. In most cases the thermal response when the current pulse was active, between minutes 5 and 8, was relatively consistent over progressive cycles. Even so, thermal variations could have caused a detectable acoustic effect. SI Figure 17 shows the acoustic and temperature response beyond minute 13 and until the end of the post-pulse relaxation (ca. minute 85). It reveals larger temperature fluctuations when this longer time-period is considered. This motivates the study of ΔToF_{rise} and $\Delta Temp_{rise}$ which are brief events, instead of $\Delta ToF_{overshoot}$ and $\Delta Temp_{overshoot}$ which are defined over a longer period (revisit Figure 2 for terminology).

Refocusing on Figure 10, the acoustic and temperature responses of the charging pulse are particularly interesting. The temperature response shows dynamic cooling of the cell, which is known to have entropic origins in the delithiation of $LiCoO_2$ [30]. This is in contrast to the multi-c-rate study of Figure 6 where heating, not cooling, was observed during charging pulses. It is possible that the cell used in the multi-c-rate study was more resistive than the one discussed here, resulting in ohmic heating which was greater than the entropic cooling. Interestingly, the ToF behaviour is the same in both cases. The ToF shifts transiently upwards, then transitions to a downwards shift and finally arrives at a new equilibrium corresponding to the new SoC. The upwards transient, when unaccompanied by a temperature rise, warrants further investigation which we reserve for future work. One hypothesis to explain this behaviour, tentatively stated, is as follows.

A lag possibly exists between the mechanical changes that take place at the anode and the cathode during the charging pulse. This lag can be the result of a heterogeneous distribution of lithium ions within the two electrodes, where the heterogeneities can be at the electrode or the particle level [38–40]. Considering the LCO cathode alone, whole-cell charging results in an increase in thickness [41] and a decrease in stiffness [42,43], both of which will tend to increase the ToF. On the side of the graphite anode, whole-cell charging also results in an increase in thickness [41], but contrary to the LCO cathode the stiffness significantly rises [29,44]. It is this stiffening of the anode which counteracts all other lithiation-induced effects and results in an eventual drop in ToF which is sustained at equilibrium. If the mechanical characteristics of the anode and cathode do not change concurrently during the charging pulse, but the anode lags the cathode, the initial rise and subsequent drop of the ToF can be explained. The lag can be the result of the aforementioned heterogeneity, which may cause the mechanical changes of the cathode to be fast compared to the anode. After a certain time, the ionic distribution homogenises both at the electrode and the particle level, and the effect of the stiffer anode on the ToF becomes dominant. Heterogeneities in the lithium-ion distribution can be reasonably expected during relatively high C-rates (1C in this case).

Contrasting charging with discharging pulses, in the latter case an overall decrease in thickness occurs, and a stiffening of the cathode. However, those are counteracted by both a lethiation-related softening of the anode and an instantaneous temperature rise. Therefore, in the discharge case any lag between the lithiation-related mechanical changes in the electrodes may be masked by the temperature rise. Future experiments should use additional equipment to measure the thickness of the whole cell *in-operando* to test this hypothesis.

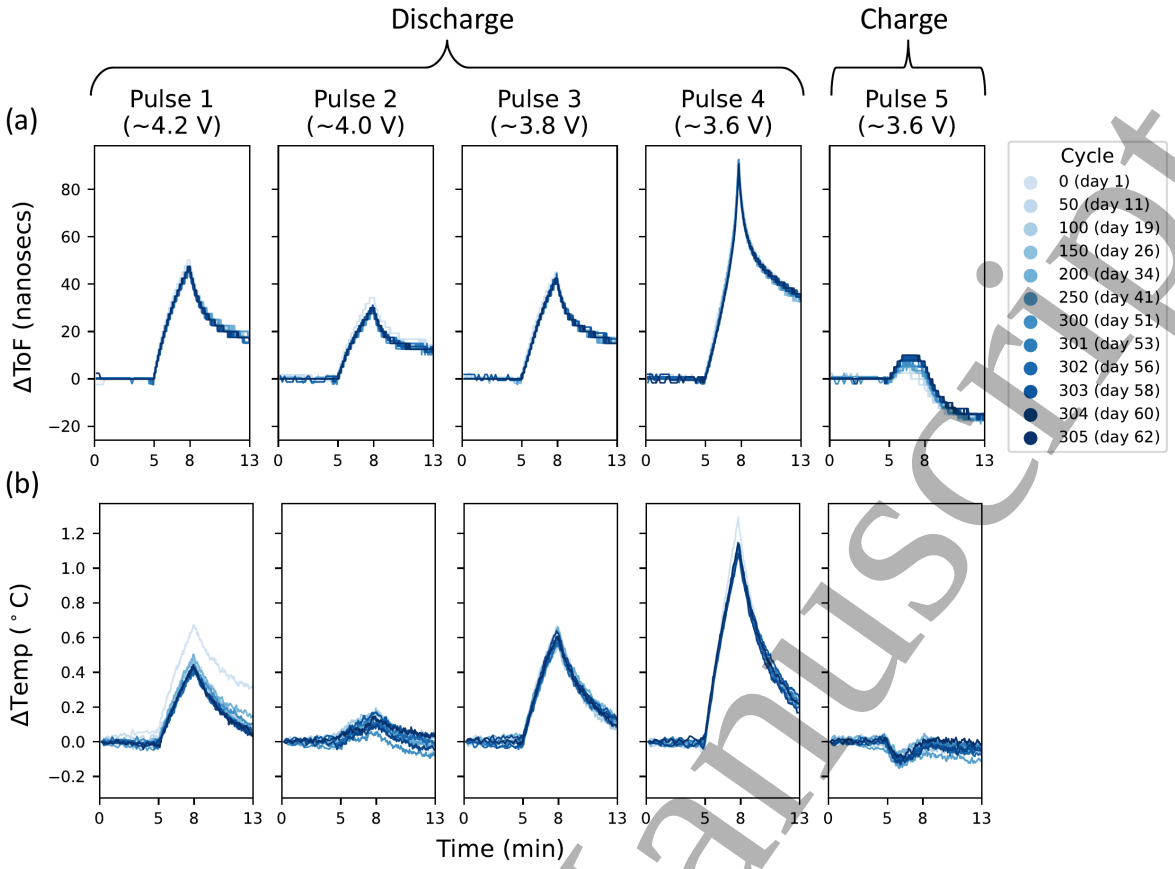

Figure 10: Dynamic acoustic response of all pulses, through life. Minutes 0–5: rest at open circuit. Minutes 5–8: 1C constant current. Subsequently: rest at open circuit. (a) Acoustic response (ΔToF) (b) Temperature response (ΔTemp). Both ΔToF and ΔTemp are baselined to start at zero for each pulse.

The four discharge pulses are analysed further henceforth. A comparison between Pulses 1, 2, 3 and 4 is not intended, as the pulses are performed at different SoCs where the mechanical and thermal characteristics of the cell differ. For example, the stiffness of the LCO cathode and graphite anode vary non-linearly with the SoC [29,42,44]. The analysis focuses instead on the evolution of dynamic characteristics for each pulse individually, over many cycles. A visual inspection of Figure 10 indicates that the ToF characteristics remain largely consistent in spite of the cell degradation, and any alteration of the dynamic acoustic response is small, especially when compared to the non-dynamic shifts discussed in Section 4.4. To evaluate whether these small changes can be uniquely related to degradation, the analysis proceeds with the isolation of dynamic features from Figure 10.

Figure 11 shows the OCV and temperature before each pulse, as well as the dynamic parameters ΔToF_{rise} and $\Delta Temp_{rise}$. We note that the OCV before each pulse was a carefully controlled parameter and was relatively consistent through-life. The respective ambient temperature parameter, T_0, could not be controlled as closely. The dynamic parameters, ΔToF_{rise} and $\Delta Temp_{rise}$, reveal non-monotonic trends with progressive cycling. The plotted regression lines aid the visual identification of these trends. As a next step in the analysis, it is desirable to compare the trends of different parameters and their relative strengths. However, comparing the trends of dissimilar parameters on their original scales would be uninformative. A fairer comparison can be performed by standardising each quantity according to its standard deviation for a specific pulse.

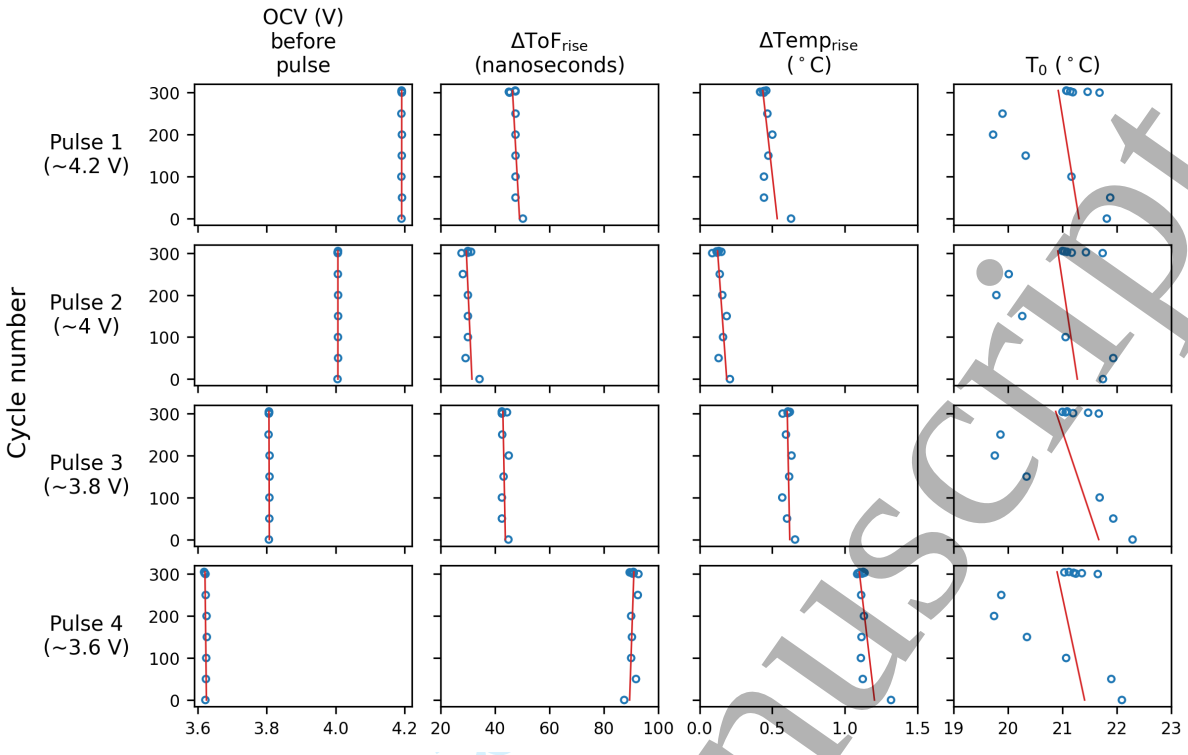

Figure 11: Pair-wise plot of cycle number vs measured parameters. Discharge pulses only. Red line indicates linear regression with the cycle number as the independent variable.

The standard deviations reveal how much scatter exists in each measured quantity. As shown in Figure 12, the careful control of the pre-pulse OCV resulted in the standard deviation being less than 2.5 mV among all pulses. The highest scatter in the OCV was associated with the pulse performed at 3.6 V. This is likely due to the longer relaxation times associated with lower voltages, which made it a more difficult voltage target to reach with good consistency while accounting for cell rest. Having quantified the experimental scatter per parameter, an immediate consideration is whether the variation of ΔToF_{rise} may be entirely explainable by the variation in $\Delta Temp_{rise}$, or if it is sufficiently higher to rule out this possibility.

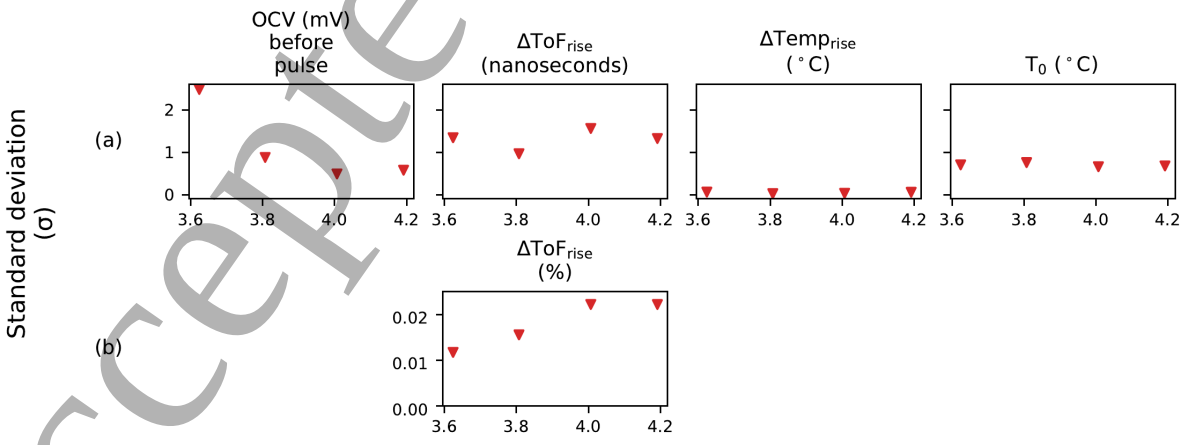

Figure 12: Standard deviations of: (a) Parameters in their original units; (b) ΔToF_{rise} as a percentage of pre-pulse values.

Table 5 lists the maximum scatter in $\Delta Temp_{rise}$ among the 4 discharge pulses, which is ca. 0.06 °C. According to the analysis of temperature effects from Section 3.2, this level of temperature variation can explain a variation in ToF of approximately 0.016 % (according to 0.28 % per 1 °C from Section 3.2). The maximum scatter in ΔToF_{rise}, in percentage units, is also listed in Table 5. Percentage values are calculated by normalising by the ToF prior to pulse initiation and are also plotted in Figure 12b. The maximum scatter in ΔToF_{rise} is 0.022 %, which is very close to what temperature effects alone could explain.

Table 5: Maximum standard deviation (among all pulses) of the dynamic parameters

Measured ΔToF_{rise} (%)	$\Delta Temp_{rise}$ (°C)	% change in ΔToF_{rise} which is explainable by the variance in $\Delta Temp_{rise}$
0.022	0.058	0.016

Beyond the levels of variation of each parameter, it is also informative to examine whether the variation contains structure in the form of trends. The direction and strength of the trends could also suggest causal links between parameters, or the lack thereof. The pair-wise trends between the cycle number and all measured parameters, standardised to zero mean and unit variance, are shown in Figure 13. The strength of each trend is quantified by the slope of the regression lines and by the Pearson and Spearman correlation coefficients, all plotted in Figure 14. The two correlation coefficients are bounded by definition to the range [-1, 1]. A Pearson correlation of -1 or +1 would reveal a perfectly linear correlation. The Spearman rank correlation quantifies the extent to which a monotonic trend is present, so values of -1 or +1 would suggest that with progressive cycling a response variable changes always in the same direction, even if not linearly. The Pearson correlation is largely equivalent to the slope of the linear regression line in this context — plotting both in Figure 14 aids the interpretation of the Pearson correlation.

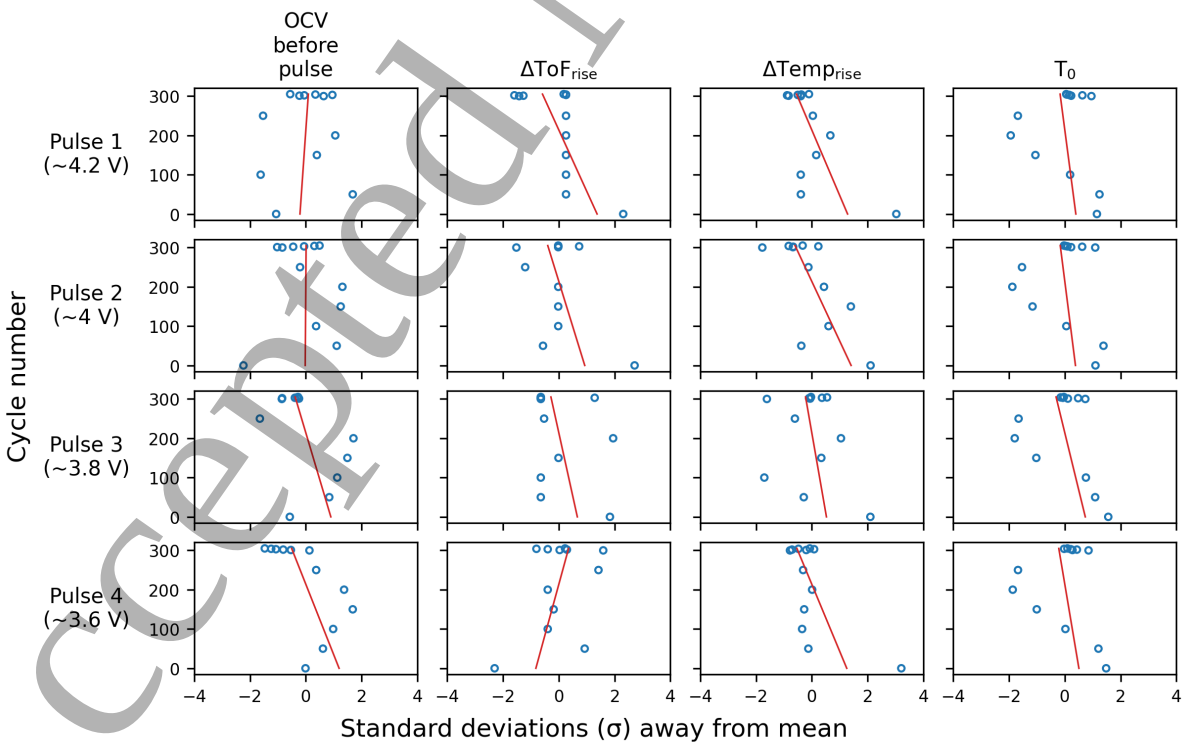

Figure 13: Pair-wise plots of cycle number vs the standardised dependent variables. Discharge pulses only. Red line indicates linear regression with cycle number as the independent variable.

A useful starting point towards interpreting Figure 14 is to observe the correlation values for the ambient temperature parameter, T_0, which is certainly independent of the cycle number. The correlation is non-zero, but it is small, with coefficient values between -0.5 and 0. For this reason, coefficients the range [-0.5, 0.5], designated by dashed lines, will be considered weak enough to not suggest a causal link to degradation. The dynamic parameter ΔToF_{rise} falls mostly within this range, with the exception of the pulses at 4.2V. The respective temperature correlations at 4.2 V, however, are equivalently strong. Therefore, there is no indication of a uniquely acoustic trend with degradation at this voltage either. It is also worth noting the large negative correlation in the pre-pulse OCV at 3.6 V. This is likely due to degradation affecting the relaxation time-constant of the cell as discussed earlier, making relaxation more sluggish when targeting the 3.6 V prior to a pulse. An influence of this is possibly seen in ΔToF_{rise}, where the Pearson correlation is near 0.5 and is positive, contrary to pulses at the other voltages. The analysis concludes that there is no strong evidence of degradation features in the dynamic acoustic response which are decoupled from temperature and voltage fluctuations and drift. It is possible that such features may emerge at greater degradation levels and capacity fade greater than ca. 15 % which was tested. If such features are present, due to the evolution of mechanical dynamics with degradation, they appear to be subtle.

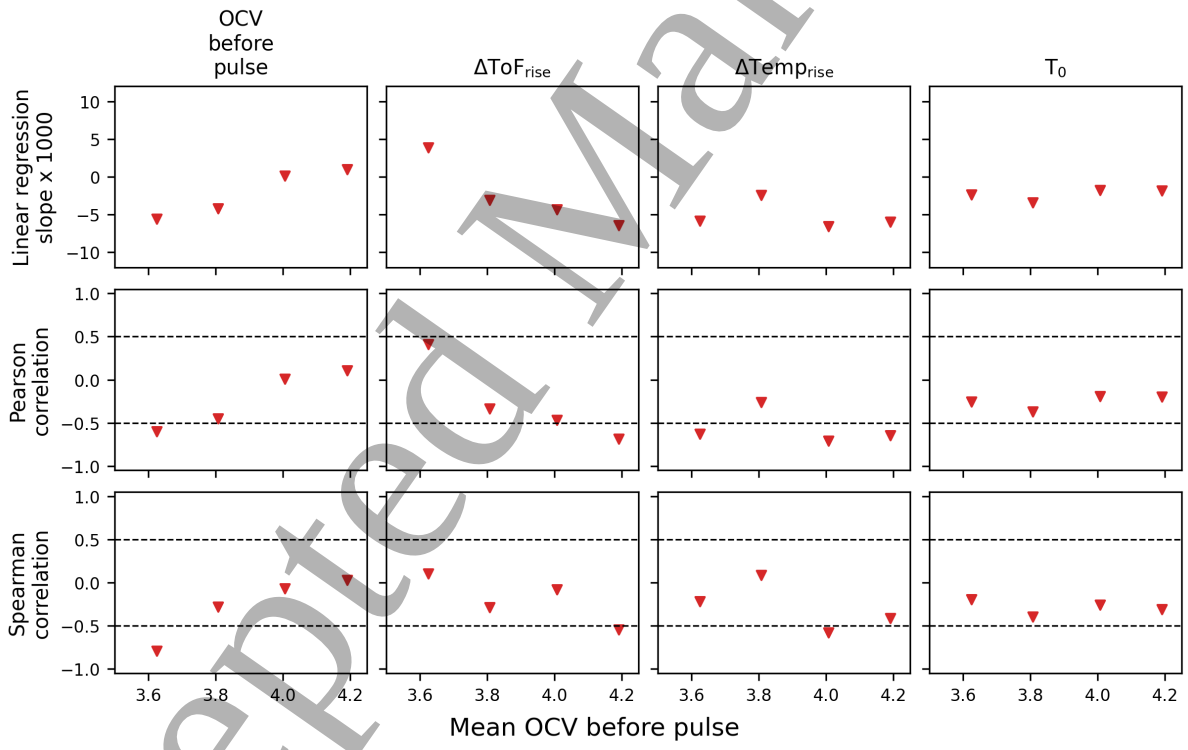

Figure 14: Summary plot quantifying the strength of pairwise trends of Figure 13.

4.6 Cautionary note concerning acoustically monitored pulse tests

A second degradation experiment was performed, where the pre-pulse OCV was not as carefully controlled. Detailed information can be found in SI Section 8, including conventional evidence of degradation, visualisations, and the statistical treatment of pair-wise trends. The second degradation

experiment also includes conventional CCCV cycling (SI Figure 21) in its reference performance tests. The evolution of dynamic acoustic characteristics with degradation was more pronounced in this second experiment (SI Figure 22); however, it was accompanied by significant drift in the voltage of each pulse. As a single-plot summary, SI Figure 24 shows the contrast between the two degradation experiments. Given that the evolution of acoustic features was found to be very subtle when carefully controlling the pre-pulse OCV, the correlations of the second experiment are believed to be artefacts of measurements taken at an inconsistent SoC. State consistency is concluded to be of paramount importance when using acoustically-monitored pulse tests to investigate battery degradation. This is stated as a point of caution to experimenters planning similar measurements.

5 Conclusions

The application of acoustic inspection to monitor battery degradation can potentially complement temperature and thickness measurements, where it must be recognised that the three signals are causally linked. The distinctive benefit of implementing an acoustic measurement is therefore case-dependent. Monitoring the evolution of mechanical properties with degradation is a useful aim; nevertheless, it was shown to be challenging due to the significant influence that temperature and thickness variations exert on the acoustic signal. Bulk shifts of the acoustic signal were shown to be substantially explainable by cell expansion, quantified by X-ray CT. This motivates the use of dynamic acoustic characteristics, as separate from absolute values, as the investigative feature. Acoustically monitored pulse tests are proposed as a useful tool to minimise the influence of thickness, and to elucidate the concurrent evolution of the temperature and time-of-flight during operation. A demonstration was made by incorporating pulse-rest sequences in the periodic monitoring of a degradation experiment. The dynamic rise parameter for the ToF (ΔToF_{rise}) was found to vary to an extent that could be entirely linked to its temperature counterpart ($\Delta Temp_{rise}$). Additionally, the formation of trends in these parameters with respect to degradation was investigated through a main effects comparison. The effect of degradation on both parameters was found to be weak and comparable. It is therefore concluded that the acoustic response in our experiments does not contain degradation markers which suggest a change in the mechanical dynamics of a degrading cell. If such markers are present, they are subtle. The degradation levels concerned are characterised by a capacity fade of ca. 15 %, most of which occurred in the first 50 cycles. An extension of our study to test greater levels of degradation is recommended. The data and code that are provided [20,21] should be useful to this end.

Additional sensitivities of an acoustic time-of-flight analysis were also exposed. Studies employing gel-type acoustic couplants can be biased due to changes in the composition of the gel, for example due to evaporation of gel contents. With respect to signal processing, the identification of waveform peaks can also introduce methodological biases, for example due to signal smoothing. These are not necessarily problematic, as they can be kept consistent for the entirety of a dataset. Nevertheless their effect is noteworthy. It was shown that a viable application for acoustic inspection could be in quantifying inhomogeneous thermal expansion through cells. This warrants further investigation into the relationship between waveform peaks and cell depth. The possible effects of the C-rate on the acoustic response, due to transient stress and strain evolution, also suggest further investigation. Charging pulses in particular were found to cause acoustic transients that were not explainable by temperature. It is recommended that future studies introduce accurate *in-operando* thickness monitoring together with the monitoring of acoustic and temperature signals.

Acknowledgements

The authors acknowledge the Faraday Institution (Faraday.ac.uk; EP/S003053/1) for the provision of funding as part of the Degradation (FIRG060), Safebatt (FIRG061), Nextrode (FIRG066) and LiSTAR (FIRG058) projects. JBR would also like to thank Innovate UK and the Aerospace Technology Institute for funding through the CEBD programme (10050803). MM acknowledges the Experimental Design Award from the STFC Batteries Network (ST/R006873/1). EG acknowledges the EPSRC for funding his studentship through the doctoral training partnership with UCL (EP/N509577/1, EP/T517793/1).

References

1. Sood, B., Osterman, M. & Pecht, M. Health monitoring of lithium-ion batteries. in *2013 IEEE Symposium on Product Compliance Engineering (ISPCE)* 1–6 (2013). doi:10.1109/ISPCE.2013.6664165.
2. G. Hsieh, A. *et al.* Electrochemical-acoustic time of flight: in operando correlation of physical dynamics with battery charge and health. *Energy Environ Sci* **8**, 1569–1577 (2015).
3. Bhadra, S., Hsieh, A. G., Wang, M. J., Hertzberg, B. J. & Steingart, D. A. Anode Characterization in Zinc-Manganese Dioxide AA Alkaline Batteries Using Electrochemical-Acoustic Time-of-Flight Analysis. *J Electrochem Soc* **163**, A1050 (2016).
4. Bhadra, S. Methods for Characterization of Batteries Using Acoustic Interrogation. (Princeton University, 2015).
5. ASTM International. E1065/E1065M-20. Standard Practice for Evaluating Characteristics of Ultrasonic Search Units. Preprint at (2020).
6. British Standards Institution. BS EN ISO 22232-2:2020. Non-destructive testing — Characterization and verification of ultrasonic test equipment — Part 2: Probes. Preprint at (2020).
7. British Standards Institution. BS EN ISO 5577:2017. Non-destructive testing — Ultrasonic testing — Vocabulary (ISO 5577:2017). Preprint at (2017).
8. Brook, M. V. *Ultrasonic Inspection Technology Development and Search Unit Design: Examples of Practical Applications*. (Wiley, New York, 2012).
9. Robinson, J. B. *et al.* Identifying Defects in Li-Ion Cells Using Ultrasound Acoustic Measurements. *J Electrochem Soc* **167**, 120530 (2020).
10. Robinson, J. B. *et al.* Spatially resolved ultrasound diagnostics of Li-ion battery electrodes. *Physical Chemistry Chemical Physics* **21**, 6354–6361 (2019).
11. Bauermann, L. P. *et al.* Scanning acoustic microscopy as a non-destructive imaging tool to localize defects inside battery cells. *Journal of Power Sources Advances* **6**, 100035 (2020).
12. Wasylowski, D. *et al.* In situ tomography of lithium-ion battery cells enabled by scanning acoustic imaging. *J Power Sources* **580**, 233295 (2023).
13. Huang, M. *et al.* Quantitative characterisation of the layered structure within lithium-ion batteries using ultrasonic resonance. *J Energy Storage* **50**, 104585 (2022).
14. Knehr, K. W. *et al.* Understanding Full-Cell Evolution and Non-chemical Electrode Crosstalk of Li-Ion Batteries. *Joule* **2**, 1146–1159 (2018).
15. Bommier, C. *et al.* Operando Acoustic Monitoring of SEI Formation and Long-Term Cycling in NMC/SiGr Composite Pouch Cells. *J Electrochem Soc* **167**, 020517 (2020).
16. Parks, H. C. W. *et al.* Direct observations of electrochemically induced intergranular cracking in polycrystalline NMC811 particles. *J Mater Chem A Mater* **11**, 21322–21332 (2023).
17. Bommier, C. *et al.* In Operando Acoustic Detection of Lithium Metal Plating in Commercial LiCoO2/Graphite Pouch Cells. *Cell Rep Phys Sci* **1**, 100035 (2020).

18. Davies, G. *et al.* State of Charge and State of Health Estimation Using Electrochemical Acoustic Time of Flight Analysis. *J Electrochem Soc* **164**, A2746 (2017).

19. Chang, W. *et al.* Measuring effective stiffness of Li-ion batteries via acoustic signal processing. *J Mater Chem A Mater* **8**, 16624–16635 (2020).

20. Galiounas, E., Jervis, R. & Robinson, J. Acoustic response of batteries during dynamic tests, through life. (2024) doi:10.5522/04/25343527.v1.

21. Galiounas, E. SonicBatt — A python package for the visualisation and processing of acoustic signals. *https://github.com/EliasGaliounas/SonicBatt* (2024).

22. Pham, M. T. M. *et al.* Correlative acoustic time-of-flight spectroscopy and X-ray imaging to investigate gas-induced delamination in lithium-ion pouch cells during thermal runaway. *J Power Sources* **470**, 228039 (2020).

23. Chang, W. *et al.* Understanding Adverse Effects of Temperature Shifts on Li-Ion Batteries: An Operando Acoustic Study. *J Electrochem Soc* **167**, 090503 (2020).

24. Owen, R. E. *et al.* Operando Ultrasonic Monitoring of Lithium-Ion Battery Temperature and Behaviour at Different Cycling Rates and under Drive Cycle Conditions. *J Electrochem Soc* **169**, 40563 (2022).

25. Popp, H. *et al.* State Estimation Approach of Lithium-Ion Batteries by Simplified Ultrasonic Time-of-Flight Measurement. *IEEE Access* **7**, 170992–171000 (2019).

26. Kinsler, L. E., Frey, A. R., Coppens, A. B. & Sanders, J. V. *Fundamentals of Acoustics (4th Edition)*. (John Wiley & Sons, 1999).

27. Gold, L. *et al.* Probing lithium-ion batteries' state-of-charge using ultrasonic transmission – Concept and laboratory testing. *J Power Sources* **343**, 536–544 (2017).

28. Robinson, J. B. *et al.* Examining the Cycling Behaviour of Li-Ion Batteries Using Ultrasonic Time-of-Flight Measurements. *J Power Sources* **444**, 227318 (2019).

29. Tavassol, H., Jones, E. M. C., Sottos, N. R. & Gewirth, A. A. Electrochemical stiffness in lithium-ion batteries. *Nature Materials 2016 15:11* **15**, 1182–1187 (2016).

30. Heubner, C., Schneider, M. & Michaelis, A. Detailed study of heat generation in porous LiCoO2 electrodes. *J Power Sources* **307**, 199–207 (2016).

31. Lazanas, A. C. & Prodromidis, M. I. Electrochemical Impedance Spectroscopy - A Tutorial. *ACS Measurement Science Au* (2022) doi:10.1021/acsmeasuresciau.2c00070.

32. Vivier, V. & Orazem, M. E. Impedance analysis of electrochemical systems. *Chem Rev* **122**, 11131–11168 (2022).

33. Iurilli, P., Brivio, C. & Wood, V. On the use of electrochemical impedance spectroscopy to characterize and model the aging phenomena of lithium-ion batteries: a critical review. *J Power Sources* **505**, 229860 (2021).

34. Tröltzsch, U., Kanoun, O. & Tränkler, H.-R. Characterizing aging effects of lithium ion batteries by impedance spectroscopy. *Electrochim Acta* **51**, 1664–1672 (2006).

35. Willenberg, L. K., Dechent, P., Fuchs, G., Sauer, D. U. & Figgemeier, E. High-Precision Monitoring of Volume Change of Commercial Lithium-Ion Batteries by Using Strain Gauges. *Sustainability* **12**, (2020).

36. Perez Estevez, M. A., Conte, F. V., Tremonti, C. & Renzi, M. Aging estimation of lithium ion cells under real-world conditions through mechanical stress measurements. *J Energy Storage* **64**, 107186 (2023).

37. Lee, J. H., Lee, H. M. & Ahn, S. Battery dimensional changes occurring during charge/discharge cycles—thin rectangular lithium ion and polymer cells. *J Power Sources* **119–121**, 833–837 (2003).

38. Finegan, D. P. *et al.* Spatial dynamics of lithiation and lithium plating during high-rate operation of graphite electrodes. *Energy Environ Sci* **13**, 2570–2584 (2020).

39. Lu, X. *et al.* Multiscale dynamics of charging and plating in graphite electrodes coupling operando microscopy and phase-field modelling. *Nat Commun* **14**, 5127 (2023).

40. Merryweather, A. J., Schnedermann, C., Jacquet, Q., Grey, C. P. & Rao, A. Operando optical tracking of single-particle ion dynamics in batteries. *Nature* **594**, 522–528 (2021).

41. Rieger, B. *et al.* Multi-scale investigation of thickness changes in a commercial pouch type lithium-ion battery. *J Energy Storage* **6**, 213–221 (2016).

42. Stallard, J. C. *et al.* Mechanical properties of cathode materials for lithium-ion batteries. *Joule* **6**, 984–1007 (2022).

43. Swallow, J. G. *et al.* Effect of Electrochemical Charging on Elastoplastic Properties and Fracture Toughness of LiXCoO2. *J Electrochem Soc* **161**, F3084 (2014).

44. Xie, H., Song, H., Kang, Y. & Wang, J. In Situ Experimental Measurement of the Mechanical Properties of Carbon-Based Electrodes during the Electrochemical Process. *J Electrochem Soc* **165**, A2069 (2018).